Modulation of Electroosmotic Flow Strength with End-Grafted Polymer Chains

Frédéric Tessier and Gary W. Slater*

Department of Physics, University of Ottawa, Ottawa, Ontario K1N 6N5, Canada

Received October 13, 2005; Revised Manuscript Received November 29, 2005

ABSTRACT: We report on coarse-grained molecular dynamics simulations of the electroosmotic flow (EOF) of an electrolyte confined in a cylindrical, nanoscopic pore. We present results for the equilibrium distribution of fluid particles and ions in the electrolyte, and we show that our computational model reproduces the well-known characteristics of EOF in the steady-state regime, in particular the well-known pluglike character of this type of flow when the Debye length is small compared to the characteristic channel size. Upon adding a number of neutral, grafted polymer chains on the interior capillary surface, we find a significant reduction of the magnitude of the EOF. We characterize the polymer coatings and further show that the observed reduction in flow strength, as a function of polymer surface coverage, is in quantitative agreement with recent theoretical scaling predictions regarding the coupling of EOF and polymer coatings in small Debye length systems. As far as we know, our results constitute the first independent, quantitative verification of these predictions.

1. Introduction

Electroosmotic flow (EOF) refers to a fluid flow induced by an external electric field applied parallel to a solid surface and occurs when a space charge builds up in the fluid near the surface. This interfacial charge may arise for different reasons, a common one being the ionization of chemical groups attached to the surface and the ensuing accumulation of counterions in an electric double-layer (EDL) near the interface (e.g., the deprotonation of silanol groups at a silica−water interface results in a net negative surface charge bound to the silica and positive counterions in solution). The EDL is often conceptually divided into an adsorbed layer (the Stern layer) and a diffuse layer of counterions; when an external electric field is applied parallel to the surface, the mobile charges in the diffuse layer are set in motion and, through viscous coupling with the uncharged fluid, eventually drag the bulk of the solution in a uniform flow.[1−5]

EOF is an efficient mode of fluid transport at small scale. Although it poses its own set of challenges, mainly regarding the control of surface chemistry, EOF is often preferred over Poiseuille (pressure-induced) flow for two main reasons: (1) The velocity of a Poiseuille flow is proportional to the square of the capillary radius; hence, the pressure gradient required to obtain decent flow rates often becomes impractical as the system size is reduced. For example, generating a 1 mm/s flow of an aqueous buffer in a 1 μm wide capillary (or 1 pL/s) already demands a pressure gradient of nearly 100 atm/cm! (2) Poiseuille flow exhibits a parabolic velocity profile, which unduly disperses material samples transported in solution. In contrast, electroosmosis generally produces a rather flat velocity profile (often called a plug flow), and for typical experimental conditions, a modest applied electric field of about 100 V/cm can reproduce the flow conditions quoted above.

A renewed interest in EOF, especially in the context of microfluidic technology, is manifest in recent publications extending EOF theory to handle time-dependent regimes[6−10] and treat completely new ideas[11,12] or proposing numerical schemes aimed at solving the constitutive equations of EOF in specific geometries.[13−15] Of a different character, in that they do not rely a priori on a continuum hydrodynamic model, molecular dynamics (MD) simulations, in which the flow emerges naturally from the integrated equations of motion of a large number of particles (representing solvent molecules, ions, etc.), have also attracted attention lately.[16−24] MD simulations provide a fundamental picture of fluid flow at the molecular scale and are likely to play a critical role in the development of nanofluidic technologies. In this article, we report on coarse-grained MD simulations of EOF in a nanoscopic cylindrical pore (or capillary), which explicitly account for the discrete nature of fluid molecules as well as hydrodynamic and electrostatic interactions; our generic approach (detailed in section 3) allows us to model large systems with nearly 5×10^4 individual particles. In contrast to some other recent EOF simulations performed in atomistic detail, we are able within our coarse-grained approach to model an electrolyte with a Debye length significantly smaller than the capillary radius; hence, the scope of our conclusions extends in part to the case of macroscopic channels.

We show in this paper that our MD model reproduces the basic characteristics of electrolytes and EOF very well, and then we consider the modification of the capillary surface with grafted polymer chains to investigate in what measure the latter is able to modulate and eventually quench the EOF altogether. This is of immediate technological relevance,[25−28] e.g., to decouple electroosmotic and electrophoretic motion of analytes in order to optimize the separation of biomolecules. Polymer coatings are routinely employed to modulate the EOF and/or to reduce the adsorption of analytes in capillary electrophoresis. These coatings exercise their control either by regulating the capillary surface charge or by enhancing viscosity near the capillary surface, or both.[29] Despite the wealth of empirical knowledge about the chemistry, processing, and performance of a large number of coatings, a fundamental understanding of the way in which adsorbed (dynamic coatings) or grafted (covalent coatings) polymer molecules modulate the EOF is still lacking. While there is considerable interest and a number of recent reports on the deformation of grafted polymers in flows near solid surfaces, we could only find one theoretical article, albeit an exceptional one, by Harden, Long, and Ajdari,[30] dedicated entirely to the coupling between the electroosmotic flow and the deformation of grafted polymer chains and the consequence

10.1021/ma0522211 CCC: $33.50
Published on Web 01/04/2006

of this coupling on the far-field solvent flow, self-consistently. Therein the authors establish some clear predictions for the deformation of polymers and for the effective bulk EOF velocity as a function of the polymer grafting density, the polymer size, and the field strength. At the end of section 2, we review the simplest limits of their theory, which serve as a baseline in the interpretation of our simulation data. As announced in our short Communication published recently,[24] this article provides elaborate details on methodology, equilibrium results for a confined electrolyte, and steady-state EOF data and ultimately offers a systematic and quantitative account of EOF modulation as a function of the coverage fraction of the polymer coating.

2. Theory

2.1. Continuum Theory of Electroosmotic Flow. Before describing our computational model and presenting our simulations results, we briefly recall the continuum theory of EOF, which relies on a combination of the Poisson equation for the electrostatic potential and the Boltzmann equation for the distribution of charges inside the diffuse layer. In general, if k refers to one of N_s ionic species present in the solution, each of valence z_k (including sign), we obtain the well-known Poisson−Boltzmann (PB) equation

$$\nabla^2\phi(\mathbf{r}) = -\frac{e}{\epsilon}\sum_{k=1}^{N_s} z_k n_{0k} \exp\{-ez_k\phi(\mathbf{r})/k_BT\} \qquad (1)$$

where $\phi(\mathbf{r})$ is the potential at position $\mathbf{r}$, e is the elementary charge, ϵ is the permittivity of the solvent (we assume it is a constant), k_B is the Boltzmann constant, and T is the absolute temperature. The n_{0k} factors are the ionic concentrations of each species in the bulk (far away from the charged wall). For the case of a symmetric univalent (1:1) electrolyte of bulk concentration n_0 confined in a system of characteristic size a, we often find eq 1 written as (in terms of the dimensionless potential $\phi^* = e\phi/k_BT$)

$$\nabla^2\phi^*(\mathbf{r}) = \frac{2e^2n_0}{\epsilon k_BT}\sinh\phi^*(\mathbf{r}) = \kappa^2\sinh\phi^*(\mathbf{r}) \qquad (2)$$

The important parameter $\kappa \equiv (2n_0e^2/\epsilon k_BT)^{1/2}$ introduced here is the inverse of the Debye length λ_D, a widely recognized measure of the extent of the diffuse charge layer (also called the Debye layer). The dimensionless combination κa is called the electrokinetic radius and amounts to the system size expressed in terms of the Debye length. The linear or Debye−Hückel (DH) approximation of eq 2, namely $\nabla^2\phi^*(\mathbf{r}) \approx \kappa^2\phi^*(\mathbf{r})$, can be invoked when $|\phi^*| < 1$ everywhere in the system. It is in this linear context that, in 1965, Rice and Whitehead (RW) first derived the properties of EOF in a cylindrical pore,[31] and their solution for the net charge density is given in terms of Bessel functions as

$$\rho(r) = -\epsilon\kappa^2\zeta\frac{I_0(\kappa r)}{I_0(\kappa a)} \qquad (3)$$

where r is the distance from the capillary axis, a is the radial position of the boundary of the diffuse layer, and $\zeta \equiv \phi(a)$ is the value of the electric potential at $r = a$. In dimensionless form, in terms of $\rho^* = \rho/n_0e$ and $\zeta^* = e\zeta/k_BT$, eq 3 becomes

$$\rho^*(r) = -2\zeta^*\frac{I_0(\kappa r)}{I_0(\kappa a)} \qquad (4)$$

If we further consider continuum hydrodynamics, we can substitute expression 3 for the charge density $\rho(r)$ into the electric body force term in the Navier−Stokes (NS) equation and solve for the fluid velocity field. Assuming that the flow is in steady state under the action of an external field E oriented along the axis of the capillary, that there are no pressure gradients, and that the fluid viscosity η is constant, the NS equation reduces to

$$\nabla^2 v(r) = -\frac{E\rho(r)}{\eta} \qquad (5)$$

Upon substituting the DH solution for $\rho(r)$ and integrating, we find

$$v(r) = -\frac{\epsilon\zeta E}{\eta}\left(1 - \frac{I_0(\kappa r)}{I_0(\kappa a)}\right) \equiv v_0\left(1 - \frac{I_0(\kappa r)}{I_0(\kappa a)}\right) \qquad (6)$$

where we have defined $v_0 \equiv \epsilon\zeta E/\eta$, the so-called "Helmholtz−Smoluchowski" velocity for the fluid far away from the charged surface (beyond the Debye layer). Note that when the ratio $I_0(\kappa r)/I_0(\kappa a)$ is replaced by $e^{-\kappa x}$ in eqs 3 and 6, we recover the appropriate solutions for a planar geometry (with x the distance from an infinite plane).

Apart from the DH linearization itself which is only reliable when $|\phi^*| < 1$, the assumption that $n_{0k} = n_0$ for all ionic species, implicit in going from eq 1 to eq 2, is in fact only valid when either the diffuse layer thickness is small compared to the characteristic system size ($\kappa a \gg 1$) or when the system is in equilibrium with a bulk electrolyte reservoir of concentration n_0. The first condition is easily violated in nanoscale capillaries, where the surface-to-volume ratio is large (i.e., there is no bulk phase inside the capillary), and although the second condition is usually met in practical settings, it is typically not enforced in simulation work, in which the total number of ions is usually fixed (NVT ensemble). In a closed nanoscale system, counterions ionized from the surface affect the ionic concentrations significantly across the entire system, and we must resort to numerical solutions of the PB equation, with values of n_{0k} determined from a self-consistent numerical solution of eq 1 under ionic conservation constraints. This point is often overlooked in the EOF literature, although it has been addressed in the context of cell models in colloid science.[32−36] We have recently presented a treatment of the issue that is both more concise and more amenable to the study of EOF in small κa systems.[37] The gist of the matter is that the PB equation for a 1:1 electrolyte can be casted in a form that resembles eq 2

$$\nabla^2 u(\mathbf{r}) = \kappa_{eff}^2\sinh u(\mathbf{r}) \qquad (7)$$

where u is simply the dimensionless electric potential ϕ^* shifted by a constant, and $k_{eff} \equiv (2n_{eff}e^2/\epsilon k_BT)^{1/2}$ is the inverse of an effective Debye length that can only be determined numerically (from boundary conditions and charge conservation integrals) and that depends on the salt concentration n_0, the wall charge density σ, and the system size a via the dimensionless combination $s \equiv |\sigma|/n_0a$. The quantity s measures the importance of the counterions dissociated from the wall, compared to that from the dissolved salt. When $s \ll 1$, the contribution of wall counterions is negligible, and we expect a bulk situation, where the effective ionic concentration away from the wall is essentially the same as the nominal salt concentration. In the opposite regime, when $s \gg 1$, the situation is dominated by the wall counterions, and both the ionic concentration and the net charge can increase well above that of the bulk approximation

values, across the whole system. It turns out that there exists a simple approximation for k_{eff}

$$\kappa_{\mathrm{eff}} \approx \kappa\,(1+s)^{1/4} \quad \text{or} \quad n_{\mathrm{eff}} \approx n_0\,(1+s)^{1/2} \tag{8}$$

where n_{eff} is then an effective salt concentration. This approximation is reliable when the wall charge σ is small enough and, most notably, even outside the linear DH regime.

2.2. Coupling between EOF and Polymer Coatings. In their self-consistent theory for the interaction between the EOF and grafted polymer chains,[30] Harden, Long, and Ajdari explore the limits of both the "mushroom" regime, in which the grafted chains are essentially isolated from one another, and the "brush" regime, in which the chains are closely packed and swell in the direction perpendicular to the surface.[38] To quantify these limits, it is customary to define a dimensionless coverage parameter $\gamma^* \equiv \gamma\pi R_g^2$, where γ is the surface polymer grafting density (the number of chains per unit area) and $R_g \equiv \langle R_g^2\rangle^{1/2}$ is the equilibrium radius of gyration of the polymers (the angled brackets denote an ensemble average). This quantity is then proportional to the fraction of the wall surface area that is covered by polymer molecules; typically, the mushroom regime corresponds to $\gamma^* \ll 1$ and the brush regime to $\gamma^* \gg 1$. We draw specific attention to the predictions of Harden et al. for the effective bulk EOF velocity v_{eff}, which can be directly extracted from simulation data. In the mushroom regime, they consider that the chains act as isolated obstacles to EOF flow generation and therefore predict, to first order, a linear decrease in the fluid velocity with γ^*:

$$v_{\mathrm{eff}} = v_0(1 - K_m\gamma^*) \quad (\gamma^* \ll 1) \tag{9}$$

where $K_m = K_m(N,E)$ is a proportionality factor which depends on the chain length N and the electric field strength E in nontrivial ways—detailed in the original paper—to account for the possible deformation of the chain in the flow field. In the brush regime, the argument relies on an analogy with the exponential screening $e^{-H/d}$ of the flow by a porous medium of height H and mean pore size d. A blob picture yields $H/d \sim \gamma^{*5/6}$, hence the scaling prediction

$$v_{\mathrm{eff}} = \frac{v_0 K_b}{\cosh \gamma^{*5/6}} \approx v_0 K_b \exp(-\gamma^{*5/6}) \quad (\gamma^* \gg 1) \tag{10}$$

Here K_b is akin to K_m and also exhibits highly nontrivial dependencies on the polymer length and the field strength, to account for the perturbation of the brush in the flow field. These dependencies are carefully scrutinized by Harden et al., but for our purpose we only need to contemplate the undeformed brush limit, in which $K_b = 1$.

We should point out that eqs 9 and 10 above are derived under the assumption that the Debye length is much smaller than other characteristic lengths in the system, such as the polymer coil size, the channel radius a, or the spacing between grafting sites, so that the diffuse charge layers are considered to be infinitely thin. Interestingly, this approximation allows one to cast the problem of grafted polyelectrolytes into a simpler one involving only neutral chains.[30] At any rate, we are curious to compare the results of our simulations, in which the Debye length is finite, against the foregoing theoretical predictions.

3. Simulation Method

Our generic model of the full electrohydrodynamic aspect of EOF is based on united-atom molecular dynamics (MD), a ubiquitous technique in the field of discrete fluid simulation (especially when macromolecules are involved, given the prohibitive computational costs of an atomistic approach when relaxation times are very long). Our system consists of about 5×10^4 spherical particles interacting via the Weeks–Chandler–Andersen (WCA) pair potential (i.e., a truncated and shifted Lennard-Jones potential, so that only the repulsive part remains):

$$U_{\mathrm{WCA}}(r) = \begin{cases} 4\epsilon\left[\left(\frac{b}{r}\right)^{12} - \left(\frac{b}{r}\right)^{6}\right] + \epsilon & r \le r_c \\ 0 & r > r_c \end{cases} \tag{11}$$

with $r_c = 2^{1/6}b$. Physical quantities in this article are quoted as dimensionless numbers and are understood to be multiplied by an appropriate combination of the natural MD units of b for length, ϵ for energy, m_f for the mass of fluid particles, and e for the elementary charge. The three first units determine the natural MD unit of time $\tau = \sqrt{m_f b^2/\epsilon}$. Because of the coarse-grained nature of the simulation, we should not attach to much importance to the interpretation of the fundamental units in terms of a specific physical system (e.g., a silica capillary filled with water at room temperature, etc.). However, to set things concretely, we can imagine that each fluid bead represents a molecule of water and that $\epsilon = k_BT$ (with $T = 300$ K), thereby establishing the rough correspondence $b \approx 0.3$ nm, $m_f \approx 18$ atomic mass units, and $\tau \approx 25$ ps. The trajectory of the particles is integrated using the velocity–Verlet algorithm with a time increment $\Delta\tau = 0.01\tau$. Most of the simulations are carried out with the same set of physical parameters, summarized in Table 1, along with corresponding approximate values in SI units according to the rough mapping established above, to provide a sense of scale. To aid in the description of our model, a snapshot of the simulation system is also provided in Figure 1.

Table 1. Simulation Parameters[a]

parameter	symbol	value (MD units)	~ value (SI units)
WCA interaction range	b	1	0.3 nm
WCA interaction strength	ϵ	1	$k_BT = 300$ K
fluid particle mass	m_f	1	3×10^{-26} kg
elementary charge	e	1	1.6×10^{-19} C
wall particle mass	m_w	3	9×10^{-26} kg
mean fluid number density	$\tilde{\rho}_f$	0.8	50 mol L^{-1}
mean wall number density	$\tilde{\rho}_w$	1.0	62 mol L^{-1}
wall spring constant	k_w	300	14 N m^{-1}
thermal energy	k_BT	1.0	300 K
bjerrum length	λ_B	2	0.6 nm
salt concentration	n_0	0.02	1 mol L^{-1}
surface charge density	σ	−0.1	−0.2 C m^{-2}
external electric field	E	3	3×10^6 V cm^{-1}
capillary radius	a	10.4	3 nm
periodic box length	L	127	38 nm
MD unit of time	τ	1	25 ps
MD integration time step	$\Delta\tau$	0.01	0.25 ps
total simulation time	t_{sim}	10^4–10^5	0.25–2.5 μs
coulomb interaction cutoff	r_{cc}	40	12 nm
FENE interaction strength	k	30	1.4 N m^{-1}
FENE interaction range	r_0	1.5	4.5 nm
DPD thermostat friction	η_{dpd}	1.5	10^{-14} g s^{-1}
total no. of particles	-	$\approx 5 \times 10^4$	$\approx 5 \times 10^4$
polymer grafting density	γ	0.01–0.15	10^{13}–10^{15} cm^{-2}
monomers per chain	M	2–20	2–20

[a] The values in MD units are understood to be multiplied by the appropriate combination of the four independent fundamental units of length (b), energy (ϵ), mass (m_f), and elementary charge (e). As an example, corresponding values in SI units are derived from the loose correspondence established for the four fundamental quantities. The polymer grafting density and the polymerization index are the parameters of most significance in this work.

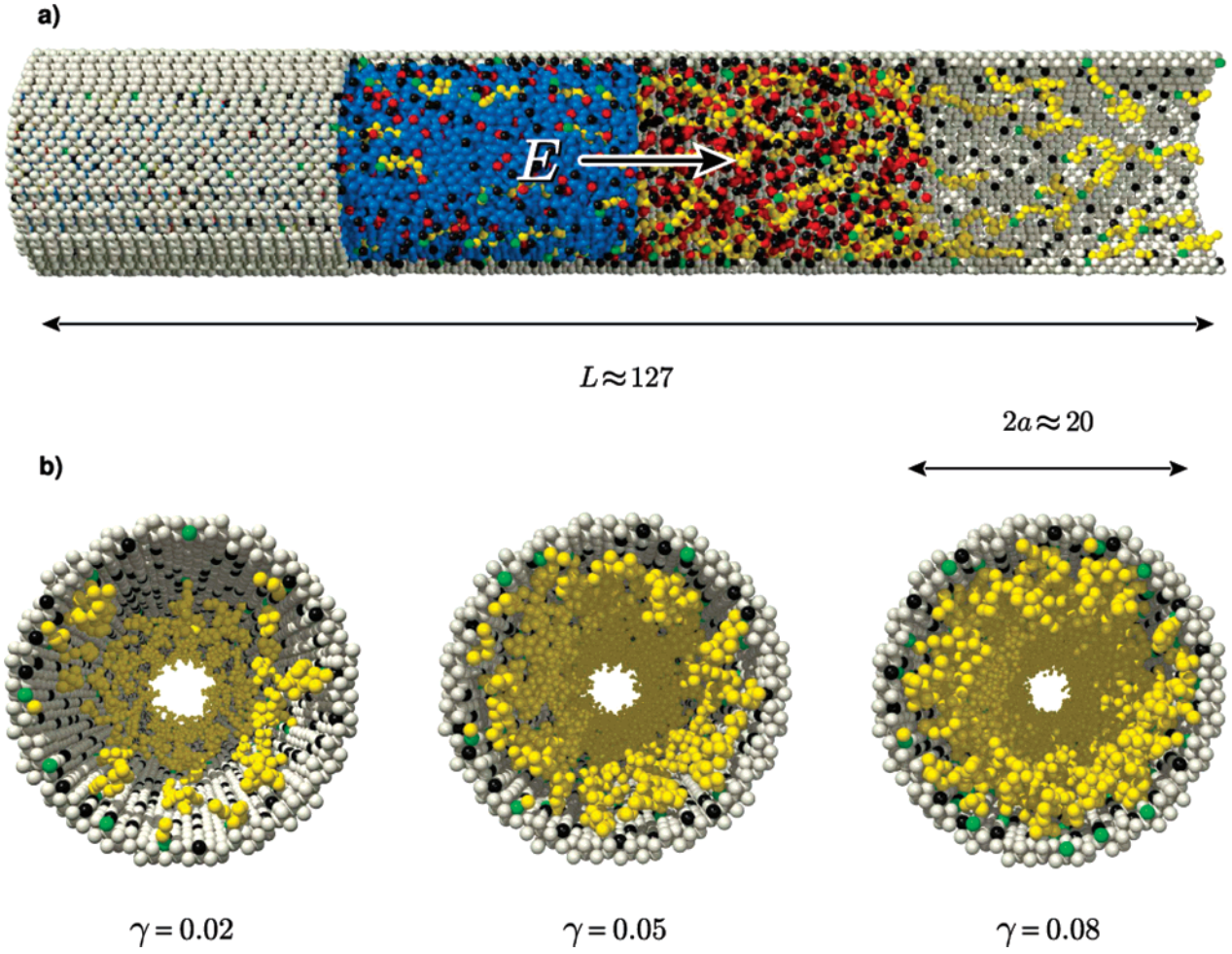

Figure 1. Visual snapshots from MD simulations of EOF control via grafted polymer chains. (a) The full length of the capillary, with some particles progressively hidden to reveal the different components of the system. Wall particles are shown in gray, fluid particles in blue, positive ions in red, negative ions in black, polymers chains in yellow, and polymer grafting sites in green. The diameter of the beads corresponds to b, the fundamental MD unit of length. Periodic boundary conditions are applied along the capillary axis, and the external field $E = 3$ is oriented toward the right. In this particular image, the grafting density is $\gamma = 0.02$, and each polymer chain comprises 10 monomers. (b) Axial snapshots, with fluid particles hidden, for three coatings of increasing polymer grafting density γ, for chains of length $M = 10$ (monomers that appear disjointed belong to chains partly outside the scope of the image). In these images, the external field is oriented out of the page.

3.1. The Capillary Wall. The capillary wall consists of a cylindrical shell extruded from an fcc lattice of mean density $\tilde{\rho}_w = 1.0$ with periodic boundary condition along the capillary axis, which models a narrow, infinitely long tube. Wall particles differ from fluid particles only in their mass m_w and in the fact that they are anchored to fixed lattice sites by simple harmonic springs with force constant k_w. We choose $m_w = 3$ and $k_w = 300$, ensuring that (1) the fundamental vibrational frequency of the wall ($\omega_w = \sqrt{k_w/m_w} = 10$) is comparable to the Einstein frequency of the fluid ($\omega_f \approx 7.8$, upon expanding the LJ potential around its minimum), so that the MD time step $\Delta\tau$ is appropriate for both; (2) the wall qualitatively behaves like a solid, in that the root-mean-square displacement of the wall particles remains below $0.1d$ (where d is the nearest-neighbor distance of the lattice; $d = (\sqrt{2}/\rho_w)^{1/3}$ in the fcc case), an empirical Lindemann criterion for melting,[39] which becomes $k_w > 3k_BT/(0.1d)^2 \approx 238$ in the current context; (3) the wall efficiently transports heat generated in the fluid by the Joule effect (i.e., we choose a small mass m_w within the limits imposed by the first two conditions). Any number of other combinations are possible, and the specific choice has little impact on the simulation outcome provided, of course, that the wall density is high enough to prevent fluid molecules from leaking out of the capillary. Given the capillary volume V (which is just the number of wall atoms removed to create the bore, divided by $\tilde{\rho}_w$) and the axial length L of the periodic box, the geometric inner capillary radius a is unambiguously determined from $V = \pi a^2 L$.

3.2. Electrostatic Interactions. To model the electrostatic aspect of EOF, we simply endow some particles with an electric charge and add between all charge pairs a truncated Coulomb interaction potential U_C, given here in dimensionless form:

$$\frac{U_C(r_{ij})}{k_BT} = \begin{cases} \dfrac{\lambda_B q_i q_j}{r_{ij}} & r \le r_{cc} \\ 0 & r > r_{cc} \end{cases} \qquad (12)$$

where r_{ij} is the distance between particles i and j, carrying charges q_i and q_j, respectively; we limit our study to univalent ions, i.e., we take $|q_i| = 1$. The Bjerrum length $\lambda_B \equiv e^2/4\pi\epsilon k_BT$ determines the relative strength of the electrostatic interaction (it corresponds to the distance at which the Coulomb energy between two unit charges is equal to the mean thermal energy). In all the simulations reported here we have set $\lambda_B = 2$, a value appropriate for water at room temperature. It is widely known that it is incorrect in 3 dimensions to impose a cutoff on the long-ranging Coulomb interaction, and Ewald summation

methods are required to take into account the contribution of the periodic images of the charges. In our case, however, the system only extends along one direction so we may consider the Coulomb interaction as short-ranged[40] for distances larger than the capillary diameter $2a$. By varying the cutoff length r_{cc} from $1a$ up to $8a$ (and increasing the periodic box length accordingly), we indeed verified that simulation results are independent of r_{cc} when it is beyond $3a$, and for the production of our final data, we chose $r_{cc} \approx 4a$, a very safe value.

The initial choice for which particles are charged is random, with the provision that the bound charges on the inner capillary surface are constrained to lie at a minimal distance from each other, so that the distribution remains more or less uniform. Pairs of opposite charges are thus applied randomly to fluid particles to model dissociated salt, and counterions opposite in charge but equal in number to the surface-bound charges are also introduced, to achieve overall electroneutrality. For all simulations we use the same salt concentration $n_0 = 0.02$ and the same surface charge density $\sigma = -0.1$ (the wall charges are negative; hence the counterions are positive). In terms of the Debye length introduced in section 2, for the largest capillary of radius $a = 10.4$ we have $\lambda_D = (8\pi n_0 \lambda_B)^{-1/2} \approx 1$, and according to eq 8, the effective Debye length is then $k_{eff}^{-1} \approx 0.91$. Thus, we expect that there will be a net positive charge and that the EOF will arise within a distance of one or two molecular diameters from the wall. Note that we do not expect to see a Stern layer of ions adsorbed on the solid surface because we use the same interaction parameters for fluid−wall and fluid−fluid interactions; at the level of our molecular-primitive model, a Stern layer would simply renormalizes the capillary radius and surface charge.

3.3. The Polymer Molecules. We model linear polymer molecules by stringing together M beads, or monomers, binding them with a finitely extensible nonlinear elastic (FENE) potential

$$U_{FENE} = \frac{1}{2}k \ln\left(1 - \frac{r^2}{r_0^2}\right) \tag{13}$$

where k and r_0 determine the stiffness and maximum extension of the bonds, respectively. We choose $k = 30$ and $r_0 = 1.5$, a widespread choice and an appropriate one to model a self-avoiding chain.[41] Another advantage of this potential over a simple harmonic one is that the polymer chain exhibits a physically realistic finite length, even under strong shear forces. In our simulations we tracked the intermonomer distance and found it to remain in the narrow range 0.97 ± 0.04. We graft each polymer to the interior capillary wall by attaching one of its ends to a random neutral wall particle with the same FENE interaction potential, and we also constrain grafting points to lie at a minimum distance from each other to limit fluctuations in the local grafting density. The polymers are initially "grown" from the grafting point in a random conformation, and in an attempt to keep the fluid density constant, we remove as many fluid particles as we add monomers (note that monomer pairs along the chain lie on average slightly closer than fluid particle pairs, so this actually implies a slight decrease in the mean fluid density). An important quantity in the analysis of the coupling between the EOF and the polymer coatings is the dimensionless coverage parameter $\gamma^* = \gamma\pi R_g^2$, which involves the equilibrium radius of gyration R_g of the chains. We have performed independent simulations to determine R_g for free chains (in bulk solution) and for isolated chains grafted on the interior capillary surface, as a function of the number of intermonomer bonds N in the molecule, with $N = M - 1$. The results are shown in Figure 2, and it is nice to see that they are consistent with the large N scaling behavior $R_g \sim N^{0.588}$ (dashed line), as well as the known scaling corrections for small N (solid line; details in the figure caption).[42] The results also indicate that, for the small chain lengths considered here, grafting has little influence on the radius of gyration of the polymer coil, and in our analysis we use the free chain R_g values.

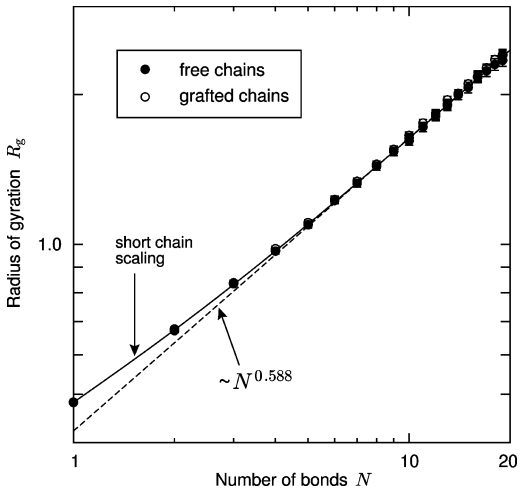

Figure 2. MD simulation results for the equilibrium radius of gyration of free and grafted FENE polymer molecules, as a function of the number of bonds N. The dashed line indicates the large N scaling relation $R_g \sim N^{\nu}$, where $\nu = 0.588$. The solid line is a nonlinear fit of a function which includes scaling corrections for small chains: $R_g = N^{0.588}(a_0 + a_1N^{-1/2} + a_2N^{-1} + a_3N^{-2})$. The values we find for the expansion coefficients a_0, a_1, a_2, and a_3 are all within 25% of published, precise values for self-avoiding walks on a cubic lattice.[42] Where visible, the error bars indicate the standard deviation in the measured R_g values.

3.4. Temperature Control. Since we are preforming non-equilibrium electrokinetic flow simulations, energy is imparted to the system by the external electric field, and in steady state this energy is converted to heat, mostly through the friction between drifting ions and the surrounding fluid and wall (Joule heating). It is therefore essential that we extract this heat from the capillary to control the temperature of our system, and to this end we combine two strategies. First, the velocity of the wall particles are rescaled periodically (typically at every 100 steps of the velocity−Verlet integration, i.e., at every τ) to keep their average kinetic energy consistent with the target temperature $k_BT = 1$. However, this is found to be insufficient (unless really small field intensities are considered, but then the flow rates become intractable in realistic simulation times), and we therefore also need to couple the fluid particles directly to a heat bath, in a way that does not bias the fluid flow and that does not require a priori knowledge of the flow profile. There exists a number of "profile-unbiased" thermostats for nonequilibrium simulations, and in our simulations we resorted to the DPD thermostat (so-called because its formulation emerged from the dissipative particle dynamics simulation method). This novel and ingenious approach boils down to rescaling the relative velocities of neighboring particles, so as to leave intact hydrodynamic interactions and the overall fluid velocity field.[43] We apply this thermostat between pairs of fluid particles, at every integration step. Finally, no thermostat is applied to the grafted polymer molecules, but their temperature is well controlled by the surrounding fluid and by their direct coupling with the wall.

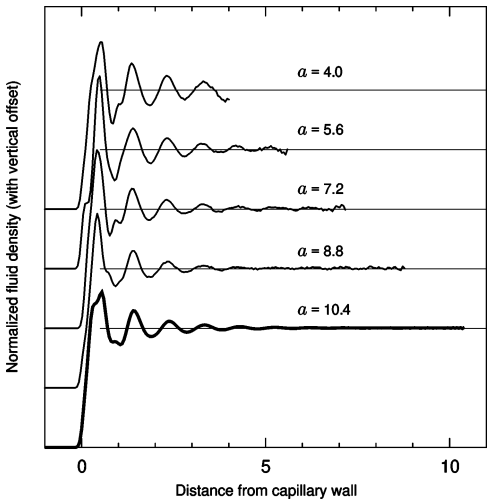

Figure 3. Normalized local fluid density $\rho_f/\tilde{\rho}_f$ as a function of the distance from the capillary wall (defined as $a - r$), for different capillary radii a, in equilibrium ($E = 0$ and $\gamma^* = 0$). The curves are offset from each other for clarity, and the horizontal lines correspond in each case to the value of the mean fluid density $\tilde{\rho}_f = 0.8$; their vertical separation of 0.5 provides a vertical scale.

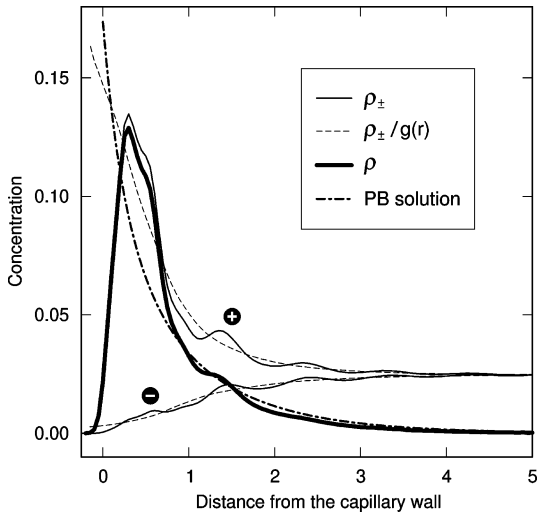

Figure 4. Details of the concentration profile for positive ions and negative ions (thin solid lines, as labeled on the graph) and for the net charge (bold solid line) near the capillary wall as a function of the distance from the wall ($a - r$), in equilibrium ($E = 0$ and $\gamma^* = 0$). The dashed curves show the ionic concentration data normalized by the local relative fluid density. The dash−dotted curve shows the net charge density predicted by the self-consistent numerical integration of the nonlinear PB eq 1 and compares favorably with the simulation results, except in the first fluid layer, where steric effects dominate.

4. Simulation Results

4.1. Equilibrium State. We first present equilibrium simulation results when there is no external field and no grafted polymers ($E = 0$, $\gamma^* = 0$). Figure 3 shows the normalized equilibrium distribution $g(r)$ of fluid particles across the capillary as a function of the distance to the capillary wall ($a - r$). The density of fluid particles shows decaying oscillations around the mean fluid density $\tilde{\rho}_f$ in the vicinity of the wall. The oscillations are very similar irrespective of the capillary radius, except for small changes in the fine structure due to the slightly different fcc lattice artifacts for different capillary radii. The values for the oscillation period (0.96 ± 0.01) and the decay length (1.2 ± 0.2) are both close to the characteristic separation of fluid particles ($\tilde{\rho}_f^{-1/3} \approx 1.08$). This layering phenomenon, due to the packing of fluid particles into layers near a solid surface, is well recognized both theoretically and experimentally.[1] Within our model it is not practical to study capillaries with a radius smaller than $a = 4.0$ because positional correlations between particles then become so strong across the whole bore as to induce intermittent crystallization of the fluid, akin to the stick−slip motion and the wall-induced glass transition observed in simulations by others.[44,45] For the rest of this work we focus on capillaries of radius $a = 10.4$ to obtain decent fluid phase in the center of the capillary and to clearly resolve the Debye length. We should reiterate here that the length of our periodic box along the capillary axis is $L = 127$, which is large enough to alleviate concerns about hydrodynamic and electrostatic self-interaction artifacts.

In Figure 4, we present results for the equilibrium charge distribution as a function of the distance to the capillary wall ($a - r$). The thick solid curve shows the net charge density ρ, obtained directly by summing the separate ionic densities ρ_+ and ρ_-, represented by thin solid lines and as labeled on the graph. The thin dashed curves give a view of the ionic concentrations $\rho_\pm$ normalized by the density oscillations $g(r)$, and the smooth profiles thus rendered show that the electrostatic and steric aspects are in first approximation separable. The PB equation therefore remains useful in predicting the charge distribution in small capillaries on a length scale smaller than the decay of density oscillations. This is confirmed most clearly by the thick dot−dashed curve, which corresponds to the net charge density profile calculated from the self-consistent solution of the nonlinear PB eq 1 (we cannot use the linear DH approximation here because $\zeta^* \approx 1.5$). The agreement with the MD simulation results is remarkable, except within one molecular diameter b of the capillary wall, as expected since the theory does not account for the finite size of the ions. The theory therefore overestimates the charge concentration in the immediate vicinity of the wall and underestimates it in the first molecular layer; however, beyond the first solvent layer the PB prediction is already quite accurate. We should note that dividing the charge density by $g(r)$ is not strictly correct because this operation does not conserve the total charge. More rigorously, we could account for packing effects in the theory by including an effective chemical potential $\mu_{pack} = \ln(g(r))$ in both exponentials in eq 1.[20] Of course, the function $g(r)$ is generally not known a priori, but it is easily extracted from a single simulation.

Beyond the right edge of the graph, toward the center of the capillary, the net charge density vanishes, and the positive and negative ionic number densities both tend toward the value $n_{eff} = 0.0247 \pm 0.0001$, which is higher than the initial salt concentration $n_0 = 0.02$. This increase is due to the absence of a bulk ionic reservoir in our system, as discussed in the paragraph leading to eq 7 in the theory above. Note that the net charge density does not necessarily vanish at $r = 0$. It does here, within the measurement uncertainty, because the Debye length is sufficiently small compared to the capillary radius. The simulation value for n_{eff} compares favorably with that prescribed by eq 8, i.e., $n_{eff} \approx n_0(1 + s)^{1/2} \approx 0.0243$, but this is partly fortuitous because the full numerical integration of the PB equation in fact predicts $n_{eff} \approx 0.0226$, which is about 10% lower. Perhaps we can attribute the discrepancy between the measured and theoretical values of n_{eff} to the structure of the fluid near the wall. According to Figure 4, ions are displaced away from the wall compared to the continuum theory prediction because of steric interactions, and it is certainly reasonable to

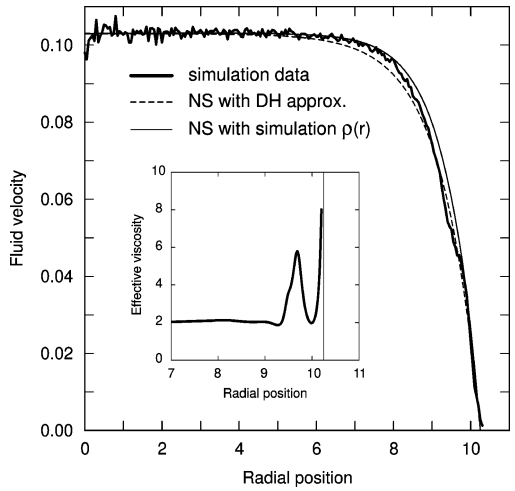

Figure 5. Steady-state EOF axial velocity $v(r)$ of fluid particles as a function of the radial position in the capillary, for an external field $E = 3$ (thick solid curve). Also shown are the prediction of the Rice and Whitehead formula based on a combination of the DH approximation for the charge density and the NS equation (dashed curve) and the numerical integration of the NS equation using the charge density determined directly from simulation data (thin solid curve). Inset: the position-dependent viscosity, as calculated from the NS equation, the charge distribution and the EOF velocity profile. The thin vertical line shows the position of the capillary wall.

expect that this has an impact on the charge density at $r = 0$, at least for the capillary size we are considering.

4.2. Steady-State EOF. We now turn to nonequilibrium simulations, in which we apply an external electric field to generate EOF, but in which the capillary walls are still free of grafted polymers. These "free-flow" results will serve as our reference scenario to calculate the reduction in the EOF strength when we consider polymer coatings in the next subsection. The electric field is included in the simulation in the form of an additional axial force qE acting on all charged particles. There is a compromise in choosing for the field strength; i.e., it must be large enough so that the velocity profiles can be resolved in a realistic computational time, yet if it is too strong it becomes difficult to control the temperature of the fluid effectively; we settle for the value $E = 3$, and we verified that under these conditions the thermostat can keep the temperature of the fluid constant across the bore and within about 1.5% of the target temperature $k_BT = 1$; the temperature gradient is located almost entirely within the capillary wall.

In Figure 5, we present the steady-state velocity profiles $v(r)$ of the fluid during EOF. The transient between the equilibrium state and the fully developed flow typically lasts about 100τ after the onset of the external field, and we only consider data points beyond 500τ in the calculation of fluid velocity profile, to ensure that they correspond to the steady-state regime. We immediately notice that we recover the expected plug-flow-like character of EOF: the profile is quite flat in the center of the capillary, and the shear is located mostly within a couple of Debye lengths from the capillary wall. We also see that our model produces a no-slip boundary condition since the fluid velocity vanishes at $r = a$. Actually, careful inspection reveals that the velocity vanishes at $r = 10.25 \pm 0.05$, which is slightly smaller than the geometrical capillary radius, and we will therefore use this reduced value in our analysis of velocity profiles. It is remarkable that, despite the irregularities in the interior wall due to the fcc lattice structure, the capillary radius inferred from geometry and from electrokinetic data agree to within 2%. The small fluctuations in the velocity profile are due to thermal noise: the typical flow velocity here is 0.1, compared to a nominal thermal velocity of $\sqrt{3k_BT/m_f} \approx 1.73$. We are thus extracting a 5% signal from the thermal motion background, and we manage to reduce fluctuations below 5% by averaging over 10^3-10^4 velocity profiles collected every 10τ during long simulations (lasting anywhere between $10^4\tau$ and $10^5\tau$).

Table 2. Three Data Sets Used in the Analysis of EOF Control with Polymer Coatings[a]

data set label	no. of data points	grafting density γ	monomers per chain M
M10	10	0.010−0.100	10
G025	10	0.025	2−20
G100	10	0.100	2−20

[a] Each set contains 10 data points, in most cases obtained from two independent simulations with the same parameters. In the text, the data sets are referred to by labels M10, G025, and G100.

We include in Figure 5 the expression derived by Rice and Whitehead for the velocity, quoted in eq 6, replacing κ by $k_{eff} \approx 1.06$, using $a = 10.25$ and taking v_0 as a fitting parameter (dashed curve; the fitted value $v_0 = 0.103 \pm 0.001$ implies a small Reynolds number $Re \approx 1$, and we are thus in a laminar flow regime). It is somewhat surprising to find that the velocity profile shape is predicted rather well by the linearized theory with adjusted parameters (it is important to note that k_{eff}, which determines the shape of the curve, is not a fitting parameter here; its value is calculated independently). We can also integrate the NS eq 5 numerically using the net charge density data $\rho(r)$ measured during EOF (different from that shown in Figure 4 because the net charge is slightly displaced away from the wall during flow) to obtain the prediction of continuum hydrodynamics without a predefined model for the distribution of charges. The predicted profile is included in Figure 5, as a thin solid line, and we see that it also describes the simulation data very well. At any rate, we cannot assess the accuracy of the predictions categorically because of possible fcc ordering artifacts and because we do not have an independent value for v_0 in the theoretical models. The variation in viscosity due to steric constraints near the wall also probably play a role. In fact, assuming continuum hydrodynamics to be valid at the molecular scale, we can estimate the local viscosity $\eta(r)$ of the fluid from electrokinetic data by writing the NS equation in cylindrical coordinates as

$$\eta(r)\nabla^2 v(r) + \frac{d\eta}{dr}\frac{dv}{dr} + \rho(r)E = 0 \qquad (14)$$

where both the charge density $\rho(r)$ and the fluid velocity $v(r)$ are directly available from simulation data (although we have to smooth the velocity profile by fitting it with a combination of a modified Bessel function and a 10th-order polynomial; FFT and running average filters do not yield curves amenable to second-order differentiation). The result of the numerical integration for $\eta(r)$ is shown in the inset of Figure 5. According to this calculation, the viscosity indeed exhibits notable variations near the wall, probably on account of the strong layering confinement of particles in the first fluid layer.

4.3. Characterization of Polymer Coatings. Given the foregoing simulation results, we are satisfied that our simulation method reproduces the features of equilibrium electrolytes and steady-state EOF very well. We now present the central point of this article, namely, a quantitative investigation of the coupling between polymer coatings and EOF, especially in light of the predictions of Harden et al. presented in the Theory section. We first summarize in Table 2 the three data sets on which we base our analysis; M10 corresponds to a data set in

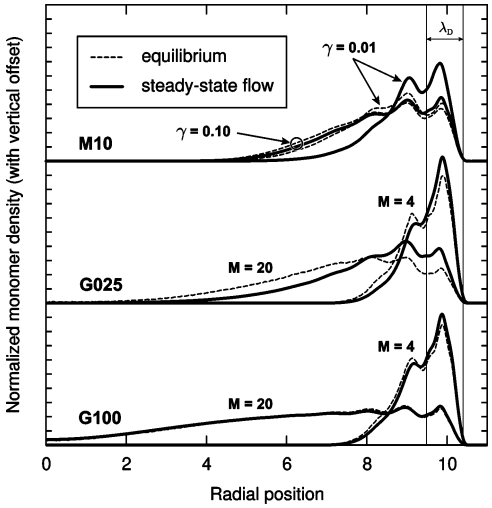

Figure 6. Radial monomer distribution in the capillary for two representative cases taken from each of the three data sets M10, G025, and G100, as labeled on the graph. We normalized the density values by γM (i.e., by the total number of monomers divided by the capillary surface) to resolve all the curves on the same scale, and we added a vertical offset between different data sets for clarity. Tick marks on the vertical axis are separated by 0.1, and the baseline for each set is evident from the curves themselves. The dash line show the equilibrium distribution when $E = 0$, i.e., when there is no flow, and the thick solid lines show the profiles during steady-state EOF, for $E = 3$. The Debye length λ_D is also indicated on the figure.

which only the grafting density is varied, for a fixed chain length, while G025 and G100 correspond to sets in which M, the number of monomers per chain, is varied, for two different grafting densities. All the other physical parameters, in particular the field strength E, assume the constant values indicated in Table 1.

The curves in Figure 6 show the normalized density of monomers as a function of radial position inside the capillary for various values of γ and M. For each data set, we show two curves: small and large values of grafting density for M10, short and long chains for G025 and G100; the curves for intermediate parameter values (not shown) interpolate well between the ones presented here. These plots characterize the polymer coating in the radial direction. The difference in profiles between the equilibrium situation ($E = 0$, dashed curves) and the steady-state flow situation ($E = 3$, solid curves) provides valuable information about the deformation of the polymers under the action of the EOF. The G100 data set indicates that for the high grafting density $\gamma = 0.1$ the monomer distribution is practically unaffected by the EOF, irrespective of chain length; the flow is not strong enough to deform these tight brushes (note that the EOF strength itself depends on the coating density, of course). On the other hand, the G025 set shows that for the small grafting density $\gamma = 0.025$ large chains incur significant deformation; the EOF pulls on the grafted chains and thus displaces the monomers toward the capillary surface. Finally, the set M10 shows a transition as the grafting density increases, for a fixed chain length: the $\gamma = 0.01$ case exhibits deformation, but the $\gamma = 0.1$ case practically none. It also clearly shows a transition from a mushroom regime to a brush regime: monomers in chains of equal lengths lie further from the surface as the grafting density increases. Assessing the flow-induced deformation of the polymer coating is important because the theoretical predictions of Harden et al. for the reduction in EOF strength due to grafted polymer chains depend on chain deformation via the numerical factors K_m and K_b in eqs 9 and 10, respectively.

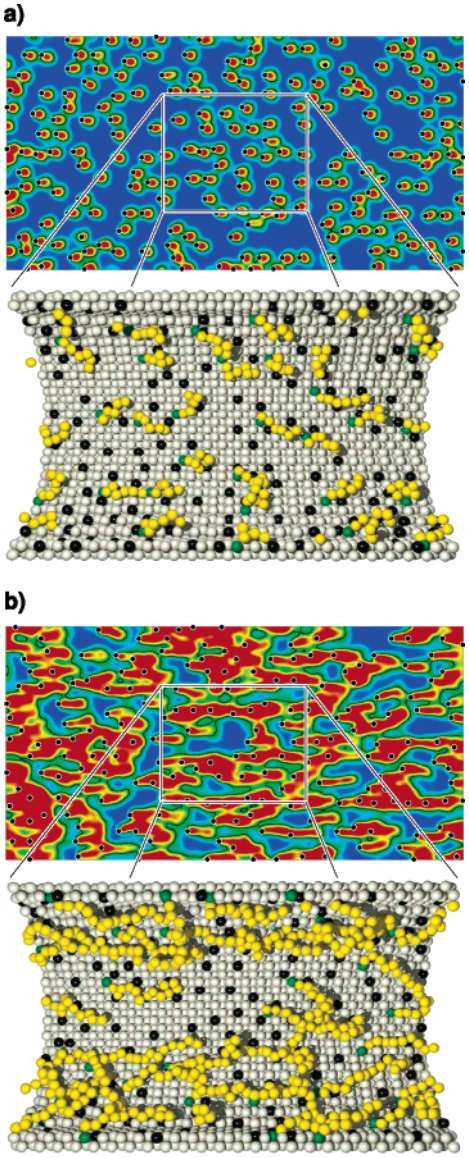

Figure 7. Visual representations of the polymer surface coatings at low grafting density $\gamma = 0.025$ (from the G100 data set), during steady-state electroosmotic flow, oriented toward the right. In the density plots, red indicates a mean monomer density of 0.5, blue represents a density of zero, and the black contours a density of 0.25. The small black points represent the anchor point of each polymer. The simulation snapshot images represent a small portion of the wall, as indicated. Wall particles are shown in gray, the wall-bound negative ions in black, the grafted chains in yellow, and the grafting sites in green; other components are hidden to reveal the structure of the coating. (a) Chains composed of six monomers are displaced from their grafting position, but they adopt conformations that are not atypical of the equilibrium state. (b) Chains composed of 14 monomers, on the other hand, incur large deformations in the direction of the flow.

A more compelling representation of the polymer coverage is provided by surface density plots such as those in Figure 7. These images show the monomer coverage density, i.e., the average number of monomers observed per unit area "above" each point of the interior capillary surface (the monomer positions are projected radially onto the surface). The red represents a mean coverage density of 0.5 or more, blue corresponds to a coverage density of zero, and the black dots show the position of the grafting sites. We show two steady-state EOF cases taken from the G025 data set: in panel Figure 7a, the chains are short and thus not affected much by the EOF. They are displaced slightly from their respective grafting points in the direction of the flow (toward the right in the figure), but

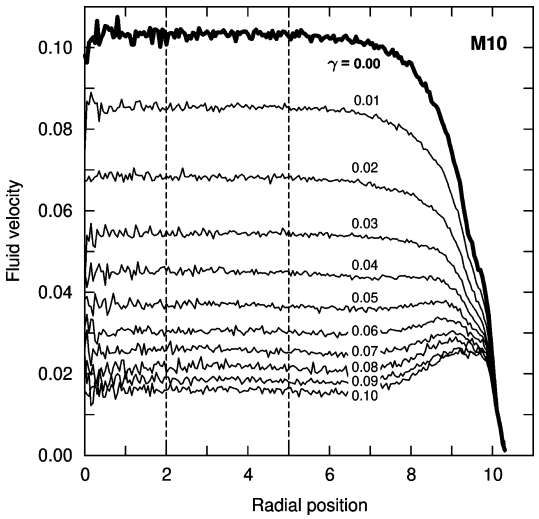

Figure 8. Molecular dynamics data of fluid velocity profiles used to determine the impact of polymer coatings on the magnitude of the EOF. We show here the data from the M10 set, with one curve for each value of the grafting density γ, as labeled on the graph. The effective bulk fluid velocity is obtained in each case from the 60 data points that lie between the vertical dashed lines.

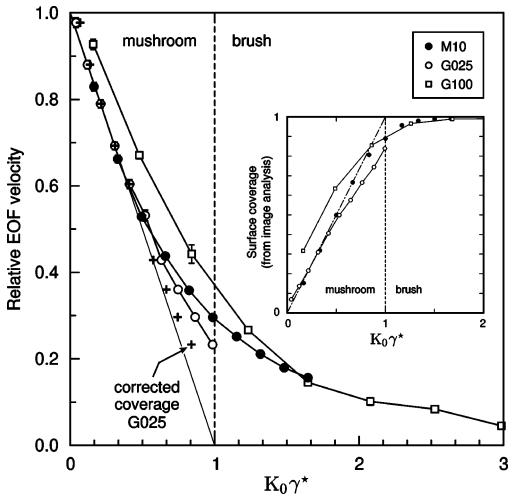

Figure 9. Relative bulk EOF velocity v_{eff}/v_0 as a function of the nominal polymer coverage density $K_0\gamma^*$, for all three data sets M10, G025, and G100. The value $K_0\gamma^* = 1$ (dashed line) divides the mushroom regime from the brush regime. The inset shows the actual coverage, obtained from the image analysis of monomer density plots (see Figure 7), as a function of the nominal coverage. Crosses on the graph show the G025 data replotted as a function of the corrected coverage values, which are more reliable in cases where the grafted polymers are deformed by the flow.

they adopt conformations that are not atypical of undeformed coils. In Figure 7b, we see how long chains are elongated in the direction of the flow by the EOF. We also remark that there is significant overlap of the chains, so that coverage fractions calculated from an isolated chain approximation are certainly overestimated. In fact, we can obtain a more reliable estimate of the polymer coating coverage fraction from a direct analysis of the density plots in Figure 7. The black contours in the images correspond to a mean monomer coverage density of 0.25; we choose to count all sites (or pixels) above this threshold as occupied (inside the contours), and the fraction of occupied sites thus yields a value for the surface coverage fraction of the coating (the choice of the value 0.25 will be motivated in the next subsection). According to this method, the situations in parts a and b of Figure 7 correspond to coverage fractions of about 0.22 and 0.65, compared to nominal γ^* values of 0.22 and 0.58, respectively. We also include in Figure 7 three-dimensional snapshots from a small section of the wall (as indicated on the figure) from the corresponding MD simulations, with fluid and solvated ions removed, to show what each coating actually looks like during steady-state EOF.

4.4. EOF Modulation with Polymer Coatings. We now present results for the reduction of the EOF due to grafted, neutral polymer chains. As our initial data, we take the average velocity profiles of the fluid as a function of the radial position r in the capillary, such as those presented in Figure 8 for the data set M10, i.e., for different values of γ at fixed chain length $M = 10$. Right away we see that there is indeed screening of the flow by the polymer coating at high grafting density: the fluid velocity is higher in the Debye layer, where the flow is generated, than in the bulk, away from the wall and the coating. We compute the effective bulk EOF velocity v_{eff} in each case by averaging over the velocity profile between $r = 2$ and $r = 5$ (to avoid the large fluctuations at small r and the shear layer near the wall), and we divide this value by the reference free-flow EOF velocity v_0 to obtain the relative EOF velocity. In Figure 9, we plot this relative velocity, v_{eff}/v_0, as a function of the dimensionless parameter $K_0\gamma^*$, where K_0 is the small deformation limit of K_m. We determine the value $K_0 = 2.20 \pm 0.05$ from eq 9 and from two data points in set G025 corresponding to $M = 4$ and $M = 6$. By comparing radial monomer density profiles with and without flow (see Figure 6), we found that these were the two mushroom regime cases that featured the least deformation of the grafted chains during EOF. The value of $K_0\gamma^*$ is thus a good measure of the surface coverage of the polymer coating for isolated chains, and accordingly, the vertical dashed line at $K_0\gamma^* = 1$ indicates the onset of the brush regime, wherein the polymer coating effectively covers the entire surface.

This is corroborated by the graph inset, in which we plot, as a function of the nominal coverage value $K_0\gamma^*$, the coating coverage fraction obtained independently from the analysis of monomer coverage density images, as detailed in the previous subsection (the only adjusted parameter in the image analysis procedure is the threshold 0.25, chosen so that the image analysis yields the same coverage as $K_0\gamma^*$ for the small deformation case $\gamma = 0.025$ and $M = 6$). Points to the right of the dash−dotted line of unit slope correspond to cases for which $K_0\gamma^*$ overestimates the value of the coating coverage (and conversely), on account of the deformation of the chains (in the sparse grafting G025 case) or because of steric interactions between chains and the emergence of the brushlike character (in the dense grafting G100 case). Fortuitously, chain deformation and steric interactions seem to compensate for each other up to a coverage fraction of about 0.8 for data in the M10 set. We remark that all the data points for which $K_0\gamma^* > 1$ correspond to coverage fractions above 0.9; hence, this threshold is indeed a good predictor of the brush regime. As mentioned above in the discussion of the radial monomer density profiles, the coatings in the M10 data set clearly show a transition from a mushroomlike regime to a brushlike one, whereas in G025 they retain a mushroom character for all chain lengths, and in G100 they mostly correspond to brushes.

On the basis of these data, let us consider the theoretical predictions of Harden et al., starting with eq 9 for the mushroom regime. We disregard the G100 data set here because the high grafting density $\gamma = 0.1$ implies that it does not include any mushroom regime data points (except perhaps for the shortest chain, but in that case the coating thickness barely spans the Debye length and the relative EOF velocity is then obviously

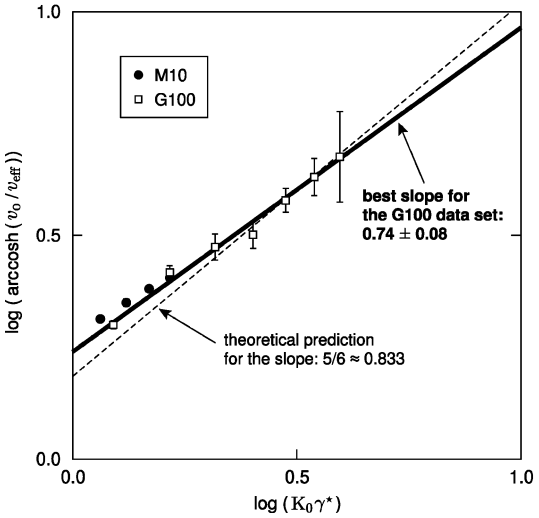

Figure 10. A plot of the brush regime data points from the M10 and G100 data sets, in a form appropriate to extract the exponent of γ^* in eq 10. The bold curve shows the best fit to the values from the G100 set, with a slope of 0.74 ± 0.08. However, as indicated by the dashed line, the highest coverage data points are certainly not inconsistent with the slope $5/6 = 0.83$ predicted from a hydrodynamic screening argument.

biased upward). Our simulation results for v_{eff}/v_0 as a function of $K_0\gamma^*$, shown in Figure 9, support the prediction that the magnitude of the EOF in the mushroom regime decreases linearly with the fraction of the surface that is covered by the polymers. Indeed, data from both the M10 and G025 sets show the same linear decrease with surface coverage. Furthermore, if we correct the coverage fraction values according to the inset, to take into account flow-induced polymer deformation of the grafted chains, we improve the agreement between data points from the G025 data set and the linear decrease of unit slope, as indicated by crosses in Figure 9.

For the analysis of the brush regime, we focus our attention on the high coverage data points of the G100 set, i.e., points for which $K_0\gamma^* > 1$. In Figure 10, we replot the relative EOF velocity so as to isolate the value of the exponent of γ^*, following the form of eq 10 (we recall that, according to the radial monomer profiles in Figure 6, brushes are essentially undeformed in the G100 data set, so we take $K_b = 1$). Upon fitting the brush regime data points with a linear function on the logarithmic graph, we find that the simulation results are best described by the equation

$$\frac{v_{eff}}{v_0} = \cosh^{-1}\{(1.74 \pm 0.08)\gamma^{*0.74\pm0.08}\} \qquad (15)$$

Thus, we find that the value of the exponent of γ^* is just beyond one standard deviation from the scaling prediction $^5/_6 = 0.8\bar{3}$ derived from the hydrodynamic screening argument. For comparison, a line of slope $^5/_6$ is also shown on the graph, and we see that the data points are qualitatively consistent with it, especially if we consider the highest coverage values. The points from the M10 set are also included in Figure 10; they do not seem to follow exactly the same trend, possibly because the brushes in M10 do incur some deformation for moderate grafting densities. In any event, the M10 curve does not extend high enough beyond $K_0\gamma^* = 1$ to be conclusive in regards to the brush regime exponent.

5. Conclusion

We carried out large-scale molecular dynamics simulations of EOF inside a nanoscale cylindrical pore and reproduced, in a quantitative way, the distribution of ions similar to what is expected from continuum theory. The oscillations of the fluid density, although manifest near the solid wall, do not appear to have a critical impact, in the sense that we can treat them separately with reasonable accuracy (provided they do not span the whole capillary pore); this is in agreement with what others have reported.[46] Classical continuum equations should not be discounted, even at the nanoscale, on the sole fact that they overlook the discrete nature of solvent molecules. The distribution of ions in the pore is predicted quite successfully by the nonlinear PB equation, provided that the effective electrolyte concentration is determined in a self-consistent way. We also considered the case where an external electric field is applied to the ions, and we reproduced an EOF velocity profile which is consistent with the predictions of continuum hydrodynamics. Note that we considered a Debye length that is about one-tenth of the capillary radius, so our findings are not necessarily specific to nanoscopic capillaries. Evidently, the scope of our conclusions is modulated by the choice of a particular simulation model. Others have performed simulations of EOF with atomistic resolution[17−20] and have reported dramatic effects pertaining, e.g., to ionic sizes and species, hydration effects, and Stern layers. The advantage of a more generic approach is precisely that it isolates the physical aspects of the problem from chemical specificity. It is also computationally more efficient, allowing for the simulation of larger length and time scales and of more complex situations that involve, case in point, polymer chains.

The main goal of this paper was to investigate the modulation of the EOF by static polymer coatings. Upon including neutral chains grafted to the interior capillary surface in our simulations, we find that the reduction of the EOF follows the theoretical predictions of Harden et al. quite well, in both the mushroom and the brush regimes (even though the theory is derived in the limit of an infinitely small Debye length). When the chains are isolated from each other, the EOF decreases linearly with γR_g^2 (with a proportionality constant $K_0 = 2.2 \pm 0.2$; it is interesting to note that we have $K_0\gamma\pi R_g^2 \approx \gamma(^3/_2 R_g)^2 \approx \gamma(2R_H)^2$, where R_H is the hydrodynamic radius of the coil). In the brush regime, the coating screens the EOF generated near the surface, and the characteristic scaling exponent 0.74 ± 0.08 that we extract from simulation data is just short of the theoretical value $^5/_6$. However, our results certainly do not rule out the value $^5/_6$, and we need to consider higher density brushes to conclude more definitely on this matter. This will require significantly larger capillaries because the longest chains considered in this work already extend close to the center of the capillary (moreover, the brush height scales linearly with N), and increasing the grafting density beyond $\gamma = 0.1$ is not practical within our model (it becomes difficult to grow the chains and the fluid density near the wall decreases significantly).

There are many directions in which to pursue this research further. In particular, we could attempt to verify more precisely the detailed predictions of Harden et al., including dependencies on the polymer length and the field strength, although we are limited in varying these two parameters by the size of the capillary and by issues with temperature control during the simulation. We could vary the Debye length to determine the behavior of the EOF in terms of λ_D/R_g and consider the case of polyelectrolyte coatings by adding charges to the monomers. We could also investigate the transient between the equilibrium state and the fully developed flow after the onset of the external field to see how polymer coatings affect the establishment of the flow in the first place. On a side note, we would maybe pay attention to the very small but systematic dip in the EOF

velocity profile at the interface of the fluid and the polymer brush (consider Figure 8, for $\gamma \geq 0.05$). Finally, our model is readily amenable to the study of dynamic coatings, which consist of adsorbed, rather than grafted, polymer chains. Intriguing experimental observations[28] concerning the magnified action of dynamic polymer coatings with reduced adsorption still lack a definitive explanation.

Acknowledgment. The authors gratefully acknowledge the support of the Natural Sciences and Engineering Research Council of Canada (NSERC) and of the National Institutes of Health (NIH) of the USA (Grant NHGRI R01 HG002918-01). F.T. also extends his gratitude to colleagues Michel Gauthier, Martin Kenward, and Jean-François Mercier for fruitful discussions. The authors are grateful to HPCVL, SHARCNET, and Westgrid for high-performance computational resources.

References and Notes

(1) Israelachvili, J. *Intermolecular and Surface Forces;* Academic Press: San Diego, 1992.
(2) Russel, W. B.; Saville, D. A.; Schowalter, W. R. *Colloidal Dispersions;* Cambridge University Press: Cambridge, 1989.
(3) Behrens, S. H.; Borkovec, M. *J. Chem. Phys.* **1999**, *103*, 2918−2928.
(4) Viovy, J. L. *Rev. Mod. Phys.* **2000**, *72*, 813−872.
(5) Karniadakis, G.; Beskok, A. *Microflows: Fundamentals and Simulation;* Springer-Verlag: New York, 2001.
(6) Erickson, D.; Li, D. Q. *Langmuir* **2003**, *19*, 5421−5430.
(7) Yang, C.; Ng, C. B.; Chan, V. *J. Colloid Interface Sci.* **2002**, *248*, 524−527.
(8) Kang, Y. J.; Yang, C.; Huang, X. Y. *Int. J. Eng. Sci.* **2002**, *40*, 2203−2221.
(9) Ren, L. Q.; Li, D. Q. *J. Colloid Interface Sci.* **2001**, *243*, 255−261.
(10) Dutta, P.; Beskok, A. *Anal. Chem.* **2001**, *73*, 5097−5102.
(11) Gitlin, I.; Stroock, A. D.; Whitesides, G. M.; Ajdari, A. *App. Phys. Lett.* **2003**, *83*, 1486−1488.
(12) Ajdari, A. *Phys. Rev. E* **2000**, *61*, R45−R48.
(13) Ren, L. Q.; Sinton, D.; Li, D. Q. *J. Micromech. Microeng.* **2003**, *13*, 739−747.
(14) Jin, Y.; Luo, G. A. *Electrophoresis* **2003**, *24*, 1242−1252.
(15) Patankar, N. A.; Hu, H. H. *Anal. Chem.* **1998**, *70*, 1870−1881.
(16) Thompson, A. P. *J. Chem. Phys.* **2003**, *119*, 7503−7511.
(17) Qiao, R.; Aluru, N. R. *App. Phys. Lett.* **2005**, *86*,.
(18) Qiao, R.; Aluru, N. R. *Phys. Rev. Lett.* **2004**, *92*,.
(19) Qiao, R.; Aluru, N. R. *Nano Lett.* **2003**, *3*, 1013−1017.
(20) Qiao, R.; Aluru, N. R. *J. Chem. Phys.* **2003**, *118*, 4692−4701.
(21) Zhou, J. D.; Cui, S. T.; Cochran, H. D. *Mol. Phys.* **2003**, *101*, 1089−1094.
(22) Cui, S. T.; Cochran, H. D. *J. Chem. Phys.* **2002**, *117*, 5850−5854.
(23) Lo, W. Y.; Chan, K. Y.; Lee, M.; Mok, K. L. *J. Electroanal. Chem.* **1998**, *450*, 265−272.
(24) Tessier, F.; Slater, G. W. *Macromolecules* **2005**, *38*, 6752−6754.
(25) Horvath, J.; Dolnik, V. *Electrophoresis* **2001**, *22*, 644−655.
(26) Dolnik, V. *Electrophoresis* **2004**, *25*, 3589−3601.
(27) Doherty, E. A. S.; Meagher, R. J.; Albarghouthi, M. N.; Barron, A. E. *Electrophoresis* **2003**, *24*, 34−54.
(28) Doherty, E. A. S.; Berglund, K. D.; Buchholz, B. A.; Kourkine, I. V.; Przybycien, T. M.; Tilton, R. D.; Barron, A. E. *Electrophoresis* **2002**, *23*, 2766−2776.
(29) Steiner, F.; Hassel, M. *Electrophoresis* **2003**, *24*, 399−407.
(30) Harden, J. L.; Long, D.; Ajdari, A. *Langmuir* **2001**, *17*, 705−715.
(31) Rice, C. L.; Whitehead, R. *J. Chem. Phys.* **1965**, *69*, 4017−4024.
(32) Dubois, M.; Zemb, T.; Belloni, L.; Delville, A.; Levitz, P.; Setton, R. *J. Chem. Phys.* **1992**, *96*, 2278−2286.
(33) Attard, P.; Mitchell, D. J.; Ninham, B. W. *J. Chem. Phys.* **1988**, *88*, 4987−4996.
(34) Attard, P.; Mitchell, D. J.; Ninham, B. W. *J. Chem. Phys.* **1988**, *89*, 4358−4367.
(35) Hansen, J. P.; Trizac, E. *Physica A* **1997**, *235*, 257−268.
(36) de Carvalho, R. J. F. L.; Trizac, E.; Hansen, J.-P. *Phys. Rev. E* **2000**, *61*, 1634−1647.
(37) Tessier, F.; Slater, G. W., submitted for publication.
(38) De Gennes, P. G. *Macromolecules* **1980**, *13*, 1069−1075.
(39) Ubbelohde, A. R. *The Molten State of Matter;* John Wiley & Sons: Chichester, 1978.
(40) Allen, M. P.; Tildesley, D. J. *Computer Simulation of liquids;* Oxford University Press: New York, 1987.
(41) Kremer, K.; Grest, G. S. *J. Chem. Phys.* **1990**, *92*, 5057−5086.
(42) Dayantis, J.; Palierne, J. **1994**, *49*, 3217−3225.
(43) Soddemann, T.; Dunweg, B.; Kremer, K. *Phys. Rev. E* **2003**, *68*, 046702.
(44) Thompson, P. A.; Robbins, M. O. *Science* **1990**, *250*, 792−794.
(45) Thompson, P. A.; Grest, G. S.; Robbins, M. O. *Phys. Rev. Lett.* **1992**, *68*, 3448−3451.
(46) Freund, J. B. *J. Chem. Phys.* **2002**, *116*, 2194−2200.

MA0522211